

Mean Seasonal Sea Surface Height Variations in and around the Makassar Strait

Ichikawa, Kaoru
Research Institute for Applied Mechanics, Kyushu University

<https://hdl.handle.net/2324/6796177>

出版情報 : Remote Sensing. 15 (17), pp.4324-, 2023-09-01. Multidisciplinary Digital Publishing
Institute : MDPI
バージョン :
権利関係 : © 2023 by the author





Article

Mean Seasonal Sea Surface Height Variations in and around the Makassar Strait

Kaoru Ichikawa

Research Institute for Applied Mechanics, Kyushu University, Fukuoka 816-8580, Japan;
ichikawa@riam.kyushu-u.ac.jp; Tel.: +81-92-583-7737

Abstract: Seasonal variations are significant in currents in the Makassar Strait, 80% of the Indonesian Throughflow (ITF) from the Pacific to the Indian Ocean, and they are in phase with both the monsoon and the sea surface height anomaly (SSHA) difference between two oceans. However, dynamics are not well discussed since gridded SSHA products within the strait are less reliable because of both over-smoothing and contamination in coastal areas. In this study, therefore, 17 years of along-track Jason altimetry data with the ALES retracker are used without grid interpolation to investigate seasonal SSHA variations in and around the Makassar Strait. All SSHA variations are in phase from the southern Celebes Sea to the northern Java Sea through the Makassar Strait, but their amplitude decreases by the distance from the southern shallow area. These amplitude modulations produce the pressure gradient force, which is maximum to the north of 4°S reaching $1.5 \times 10^{-6} \text{ ms}^{-2}$, and that would be balanced with the bottom friction of the upper-layer ITF velocity, rather than the wind stress whose magnitude $5 \times 10^{-8} \text{ ms}^{-2}$ is too small. The SSHA difference between the two oceans is in phase but is isolated from the Makassar Strait by adjacent uncorrelated SSHA variations.

Keywords: Makassar Strait; Indonesian throughflow; seasonal SSH variations; ALES retracker; along-track Jason altimetry data; Labani Channel; sea level difference between the Pacific and Indian Ocean; dynamic balance in shallow straits; Kelvin waves; aliased K_1 constituent



Citation: Ichikawa, K. Mean Seasonal Sea Surface Height Variations in and around the Makassar Strait. *Remote Sens.* **2023**, *15*, 4324. <https://doi.org/10.3390/rs15174324>

Academic Editors: Xiaoli Deng, Jérôme Benveniste, Stelios Mertikas and Vladimir N. Kudryavtsev

Received: 2 July 2023

Revised: 4 August 2023

Accepted: 30 August 2023

Published: 1 September 2023



Copyright: © 2023 by the author. Licensee MDPI, Basel, Switzerland. This article is an open access article distributed under the terms and conditions of the Creative Commons Attribution (CC BY) license (<https://creativecommons.org/licenses/by/4.0/>).

1. Introduction

The Makassar Strait connects the Celebes Sea and the Java and Flores Seas (Figure 1), and approximately 80% of the southward Indonesian throughflow (ITF) from the Pacific Ocean to the Indian Ocean is considered to pass this strait [1]. Most areas of the southern part of the strait are shallower than 50 m, so deeper layers of the ITF are confined to the narrow (approximately 45 km width) Labani Channel. Long-term mooring with current meters in the Labani Channel has revealed that the currents in the Makassar Strait change in various time scales, but they have dominant seasonal variations, although semi-annual variations are also found in layers deeper than 300 m [1].

Many researchers have investigated the ITF variations and related them to the sea level differences, or the pressure gradient force, at various time scales. Daily gridded satellite altimetry sea surface height (SSH) products are used in [2] to obtain the SSH anomaly (SSHA) difference between the Celebes Sea and the Java Sea to discuss the Madden-Julian Oscillation (MJO). Term balances in the equation of motion in the along-strait direction reveal that both northward along-strait wind stress and northward pressure gradient over the Makassar Strait during the active phase of the MJO events will accelerate the northward ITF in the upper layers. Meanwhile, dominant seasonal variations in the upper-layer ITF have been found well correlated with both monsoon wind variations and the seasonal SSHA differences between the southwestern Pacific Ocean and the northeastern Indian Ocean that are also estimated from gridded satellite altimetry products [3,4]. Namely, the current in the Makassar Strait increases the northward component, or the southward ITF becomes weakened during the northwest Australian-Indonesian monsoon from December

to March, and the SSHA in the northeastern Indian Ocean becomes higher than that in the southwestern Pacific Ocean. In addition, annual SSHA variations at three points in the central Makassar Strait, the southwestern Celebes Sea, and the northeastern Java Sea in another gridded altimetry product have been investigated to reveal that the seasonal SSHA gradient in the Makassar Strait is in phase with the SSHA difference between the Pacific and Indian Ocean [5].

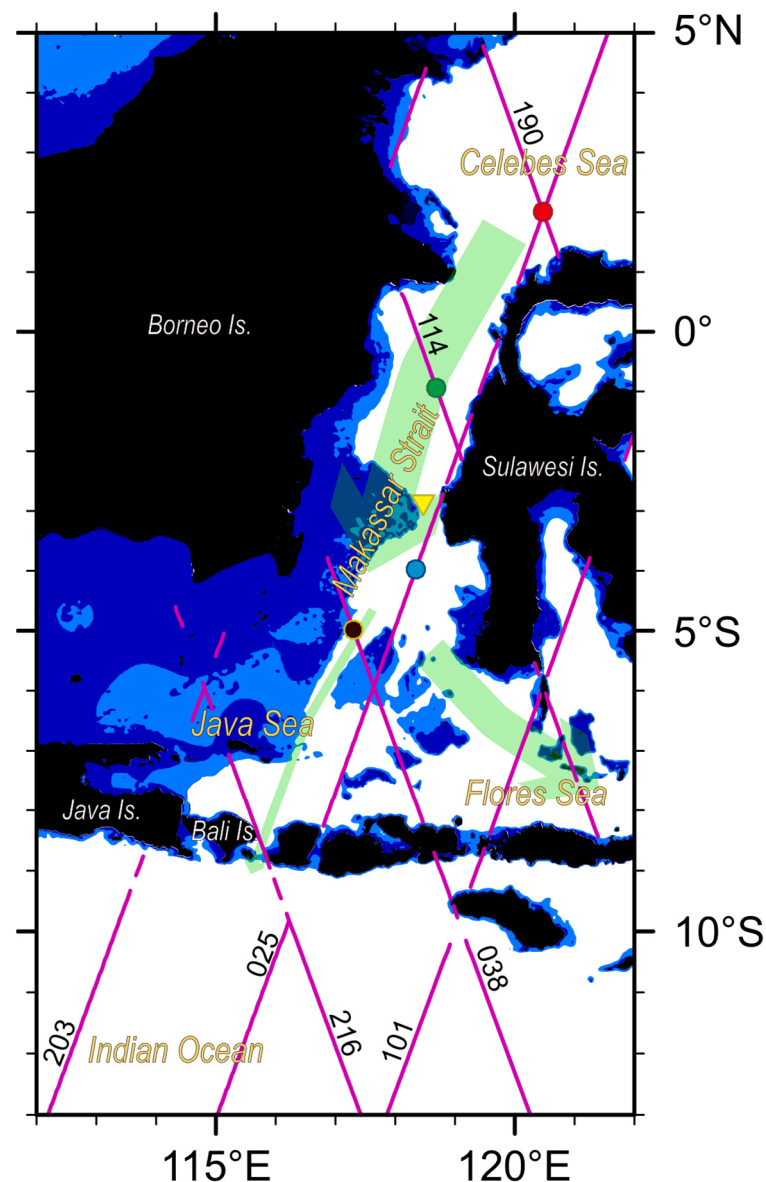


Figure 1. Location of data points in the Makassar Strait. The schematic ITF pathway in the strait is shown using bold green arrows. Purple lines with numbers show Jason's tracks (from 2002 to 2019). The seasonal SSH variations at 2°N along Track 190 (red circle), at 1°S along Track 114 (green circle), at 4°S along Track 025 (blue circle), and at 5°S along Track 038 (black circle) are used. A yellow triangle in the Labani Channel shows the location of the current meter mooring site in [1]. Areas with depths shallower than 50 m and 300 m are shaded with dark and light blue colors, respectively.

However, descriptions of these seasonal variations within the Makassar Strait are rather qualitative, and quantitative dynamic term balances, as investigated for the MJO in [2], are not well discussed. In addition, the relationship between the pressure gradient force within the Makassar Strait and the external larger-scale SSHA difference between the Pacific and Indian Ocean is not understood well, although they are known in phase [4]. For

example, if the seasonal pressure gradient force variations between the Pacific and Indian Ocean directly produce the SSHA gradient in the Makassar Strait, uniform SSH gradient over the whole Celebes and Java Seas between the Pacific and Indian Ocean would be expected, but they have not investigated yet.

One reason the seasonal SSH variations within the Makassar Strait are not quantitatively discussed would be that standard satellite altimeter products are less reliable in a narrow strait than in open oceans [6,7]. Conventional satellite altimeters assume homogeneous reflection of microwave pulses at the sea surface, but this condition may not hold in areas close to coasts because of the occurrence of inhomogeneous microwave reflections by, e.g., lands, ships, and calm water in semi-closed ports [8]. Therefore, in a narrow strait where most areas are close to coasts on both sides, the quality of altimetry observations is low. In addition, in the calm Indonesian Seas, small areas of smoother sea surface roughness (as known as “slicks”) that significantly reflect microwaves are often found even away from lands [9,10], so that the quality of standard altimeter datasets are further lower in this region.

In gridded SSH products, interpolations in time and space would relax those quality problems by filtering out outliers using the surrounding SSH data. In addition, spatial interpolation in gridded SSH products would also overcome problems with a less dense distribution of observation points [11]. However, in coastal straits, SSH distribution within the strait could be strongly controlled by topography so that it could be significantly independent of SSH observations outside the strait. High-frequency ocean radar systems, which can provide dense observations of surface ocean currents in a limited coastal area, have revealed that currents in straits are so locally confined that simple spatial interpolations of sparse data coverage would not be able to account for this complexity [6,12]. In the Makassar Strait, which includes significant shallow bottom topography (Figure 1), simple spatial interpolation in a gridded SSH product may erase characteristic SSH signals within the strait by referring uncorrelated data outside unless some sophisticated data assimilation techniques with complex physics accounts were used. This could be another reason dynamic term balances are not discussed quantitatively in the Makassar Strait.

Recently, however, new products have been developed to increase data availability in coastal areas [13,14]. The use of these coastal SSH products would enable us to discuss the dynamics of the seasonal SSH variations in the Makassar Strait quantitatively. The targets of this study are, therefore,

1. We use 17-year Jason coastal altimetry SSH products that can provide denser observation points with better quality, even in the narrow Makassar Strait.
2. We use those SSHA observations without spatial grid interpolations, although the data points become irregularly distributed.
3. Using quantitative SSHA gradient values, we investigate dynamic term balances of seasonal variations within the Makassar Strait.
4. By extending the study area outside the Makassar Strait (Celebes Sea, Java Sea, Flores Sea, and Pacific and Indian Ocean), we investigate the distribution of seasonal SSHA gradients around the Makassar Strait.
5. Then, we investigate the relationship between the seasonal SSHA gradient in the Makassar Strait and the seasonal SSHA difference between the Pacific and Indian Oceans.

We describe materials and methods in Section 2, and then seasonal SSHA variations and dynamic balances within the Makassar Strait will be discussed in Section 3. The seasonal SSHA variations around the Makassar Strait will be described in Section 4 to investigate the relationship to the SSHA difference between the Pacific and the Indian Ocean. Factors that may affect the results will be discussed in Section 5, and a summary and conclusions will be provided in Section 6.

2. Materials and Methods

Since we dare to use non-gridded SSH data in this study, errors in a single SSH observation at a point may not be smoothed out using the surrounding SSH data. Therefore,

the quality of single observations needs to be higher. In this study, therefore, we use the Adaptive Leading Edge Subwaveform (ALES) retracker Version 55 applied to Jason-series altimetry SSH data (Jason-1 from January 2002 to July 2008; Jason-2 from July 2008 to February 2016; Jason-3 from February 2016 to April 2019). Although the TOPEX/Poseidon satellite took the same tracks as the Jason series, no retracked data are available for the TOPEX/Poseidon mission. The ALES SSH data were produced by DGFI-TUM and distributed via OpenADB (<http://www.openadb.dgfi.tum.de>, accessed on 15 January 2023). ALES dataset has been adjusted with fundamental range corrections used in standard products, like tropospheric, ionospheric, sea state bias, and dynamic atmosphere corrections. Tidal corrections (solid earth, load, ocean, and pole tides) are also applied; for ocean tides, the Empirical Ocean Tide (EOT) model produced by DGFI-TUM is used [15]. More details on the retracker and the product are available in [16–18].

We exclude all data that satisfy any of the conditions listed in Table 1, as suggested by the data provider. In order to further reduce noises, the along-track 1-Hz SSH data are smoothed over five points (approximately 35 km long track) and nine cycles (approximately 90 days) with Gaussian weight function $\exp\left[-\left(\frac{dr}{L}\right)^2 - \left(\frac{dt}{T}\right)^2\right]$, where dr is the along-track distance, dt is the temporal difference, L is the spatial smoothing scale (35 km), and T is the temporal smoothing scale (90 days); this process smooths out small-scale variations (thus called the Gaussian filter). Unlike the grid interpolation, which refers to far and sparse observations on different satellite tracks that may be located outside of bays or straits, the along-track smoothing can reduce the noises of each observation by referring to dense distributions (7 km separation) along the same track, and thus suitable for coastal studies [6,7,9]. Note that the temporal smoothing also reduces residual errors in the corrections of aliased tides, except for the K_1 constituent whose aliased period is 173 days (e.g., [19]).

Table 1. Excluding conditions for ALES SSH data.

Values	Conditions
Distance to Coast	Less than 3 km
Absolute value of SSH anomaly	Larger than 2.5 m
Significant Wave Height	Higher than 11 m
Standard deviation in 1 sec	Larger than 0.2 m

The ALES SSH data refer to the mean sea surface data from the DTU15 model [20], but in this study, we only use the SSHA data $Z(r, t)$ from the 17-year temporal mean. Near-annual SSHA variations $Z^{na}(t)$ are then extracted from the time series of the SSHA data $Z(r_0, t)$ at a point r_0 by removing both variations longer than 13 months ($T = 390$ days) and shorter than 10 months ($T = 300$ days) using Gaussian filters (Figure 2a). Namely, long-term variations $Z^L(t)$ are first determined from $Z(r_0, t)$ by the 13-month Gaussian filter. Then, the 10-month Gaussian filter applies to the residual component $Z(r_0, t) - Z^L(t)$ to extract the near-annual SSHA variations $Z^{na}(t)$, and the residual component $Z(r_0, t) - Z^L(t) - Z^{na}(t)$ becomes the short-term variations $Z^S(t)$.

In Figure 2a, the largest magnitude of variations is found in the short-term variations Z^S . The root-mean-squared (RMS) values for Z^S , Z^{na} , and Z^L in Figure 2a are 0.15 m, 0.08 m, and 0.05 m, respectively. The short-term variations Z^S obviously include nearly semi-annual variations, but as seen in Figure 2a, the dates of peaks and troughs are not locked by annual year days but shifted during a long period. Indeed, the dominant period of Z^S is approximately 173 days, so they would be dominated by aliased tidal errors of the K_1 constituent.

Meanwhile, as shown in Figure 2b, all near-annual SSHA variations Z^{na} show phase-locked similar seasonal changes, although they behave slightly differently each year. For example, maximum peaks are found in January or February, but the peak in 2011 around the year day 30 is significantly larger than those in the other years. Similarly, the mini-

num troughs are found in the boreal summer, but the trough in 2006 around the year day 240 deviates from those in the other years. These deviations could be related to the enhanced short-term variations Z^S or long-term variations Z^L , which could be caused by some interannual events such as El Nino/Southern Oscillation (ENSO) or Indian Ocean Dipole (IOD). However, they might be caused by unexpected data gaps in late 2006 (Figure 2a). Therefore, we only focus on the 17-year mean seasonal variations in this study. The mean seasonal SSHA variations η are determined by taking the 17-year monthly mean from over 50 samples (three cycles in a month in a year). The data point will be discarded if the number of cycles used is less than a half of full observations.

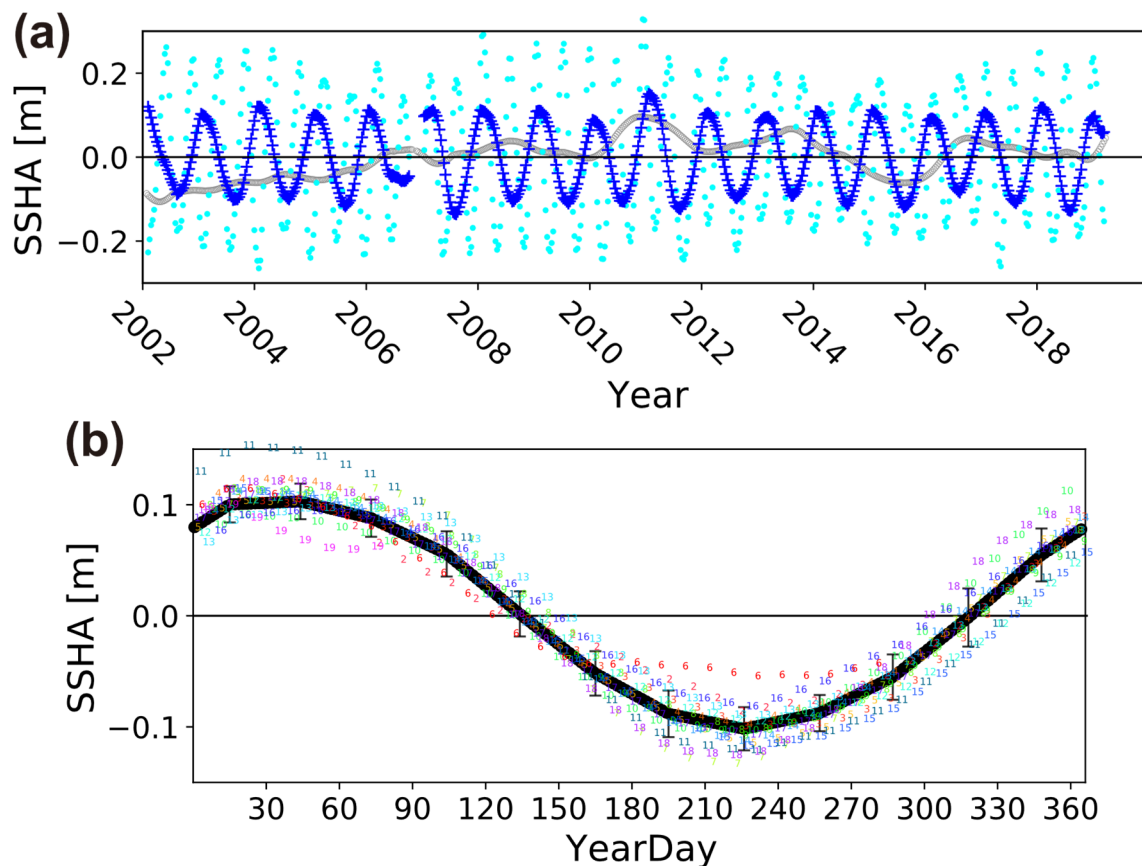


Figure 2. (a) Various SSHA components at 5°S , 117.3°E in the Makassar Strait (marked by the black circle in Figure 1). Near-annual variations Z^{na} are plotted using blue crosses. Short-term variations Z^S and long-term variations Z^L are plotted using light-blue dots and gray circles, respectively. (b) The same near-annual SSHA variations Z^{na} plotted against year days. Colored numbers plotted show years of observations after 2000; a unique color is used for each year. Monthly mean SSHA values η over 17 years, and their standard deviations are shown with black lines.

To investigate dynamic balance with the pressure gradient force because of the SSHA gradient, we also use wind stress data and the ITF velocity data. The hourly velocity measurements from moorings maintained in the Labani Channel in the Makassar Strait from 1996 to 2017 are downloaded from <https://doi.org/10.7916/d8-p78a-zm51>, accessed on 10 January 2023 [21]. The data has been re-sampled at 20 m depth intervals between 40 and 760 m. The location of the mooring was marked using a yellow triangle in Figure 1 at 2.8647°S , 118.4629°E . Following the past study [1], the along-strait direction is defined as the axis rotated clockwise from the north by 10° . Note that no data was available for approximately two years, from July 2011 to August 2013.

Monthly averaged sea surface temperature (SST) and wind stress (τ) values in the Makassar Strait (centered at 1°S , 118.5°E) are extracted from 0.25° -gridded “third-generation

Japanese Ocean Flux Data Sets with Use of Remote Sensing Observations" (J-OFURO3) version 1.1 data [22]. The duration of SST data is from 1988 to 2017, while that of the wind stress τ is from 1991 to 2017. The along-strait component of the wind stress is extracted similarly to the ITF velocity.

We extract the mean seasonal variations from the time series of the ITF along-strait velocity, SST, and the along-strait wind stress, similar to the SSHA Gaussian filters. Although the durations of all datasets are different, we assume that all these durations are long enough to assume the mean seasonal variations of each dataset are not affected by either slight differences in durations or the presence or absence of interannual events such as ENSO and IOD.

3. Variations within the Makassar Strait

The non-gridded mean seasonal SSHA variations at four points in the Makassar Strait and the Celebes Sea (Figure 1) are plotted in Figure 3a. They are on different satellite tracks, so they are determined independently, but all variations are found in phase; positive values are found during the northwest Australian-Indonesian monsoon, December to March, while negative values are found during the southeast monsoon, June to September. Their half ranges from the minimums to the maximums, or amplitudes, are significantly larger than their standard deviations. The amplitude of these in-phase variations is monotonically increased from the northern points (2°N and 1°S) to the southern points (4°S and 5°S), as suggested in [5].

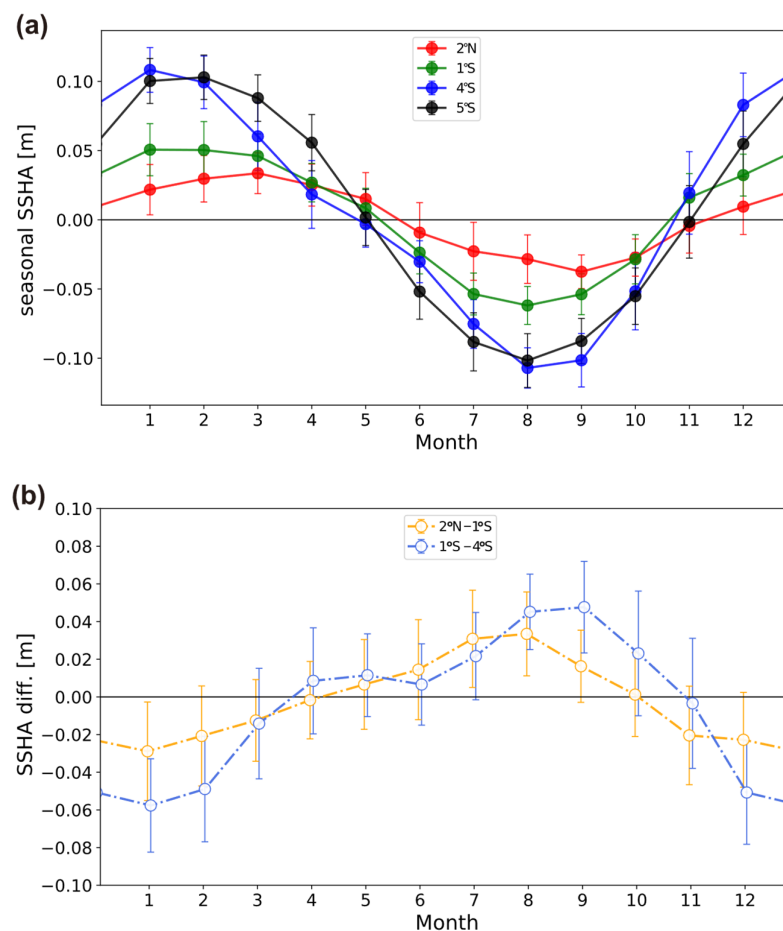


Figure 3. (a) Mean seasonal SSHA variations with standard deviations at four points (5°S , black; 4°S , blue; 1°S , green; 2°N , red) in the Makassar Strait and the Celebes Sea, whose locations are shown in Figure 1. The black line is the same as in Figure 2b. (b) Seasonal variations of the SSHA differences between 2°N and 1°S (red) and 1°S and 4°S (blue). Vertical bars show the rooted sum of squared standard deviations.

However, as shown in Figure 3b, the SSHA differences in the southern part of the Makassar Strait between 4°S and 1°S are significantly larger than ones in the northern part between 1°S and 2°N, whereas the spatial length of both pairs is approximately the same 400 km. This suggests that the SSHA gradient is not uniform in the Makassar Strait, and the larger SSHA gradients would be found to the north of 4°S or near the Labani Channel, where most areas of the strait are shallower than 50 m (Figure 1).

The mean seasonal SSHA variations in the southern part of the Makassar Strait at 5°S are compared to the other seasonal variations in Figure 4. The SSHA variations (black bold line) agree well with the opposite phase of the along-strait wind stress component (blue broken line) with the significant Pearson correlation coefficient (CC) = −0.95. During the northwest (or southeast) monsoon from December to March (June to September), the along-strait wind component in the Makassar Strait is southward (northward). Similar phase variations with the SSHA (CC = 0.82) are also found in the along-strait ITF velocity component at the 40 m depth (yellow chain line), as the northward (or southward) anomaly is found during the northwest (southeast) monsoon, although the northward ITF anomaly ends slightly earlier in March than the end of the positive SSHA in May. Note that the seasonal SSH variations at 4°S (blue line in Figure 3a), which is closer to the mooring site, show an earlier end of the positive SSHA in April and better CC = 0.92. All those similarities qualitatively agree with the past studies [1,3,5].

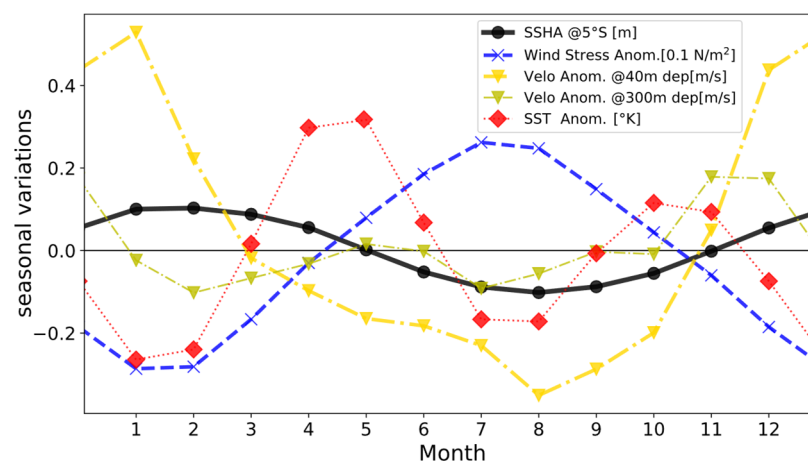


Figure 4. Various mean seasonal variations in the Makassar Strait. A solid black line shows SSHA variations in the meter unit at the black point (5°S) in Figure 1. The anomaly of the along-strait wind stress component in 0.1 N m^{-2} unit is shown using a broken blue line. A red dotted line is for the SST anomaly in the °K unit. The seasonal variations of the along-strait ITF velocity component observed at the mooring site (yellow triangle in Figure 1) in the Labani Channel are plotted in m s^{-1} unit using yellow or green chain lines; values at the 40 m depth are indicated using yellow triangles, while those at the 300 m depth are plotted using green triangles.

Meanwhile, the ITF velocity at the 300 m depth (green chain line) shows significantly different variations. Semi-annual variations with peaks in November and May are significantly present [1,3,23], suggesting that the ITF variations in the deeper layers are related to some other factors than the seasonal SSHA variations within the Makassar Strait.

Similarly, the seasonal SST anomaly variations (red dotted line) also show significant semi-annual variations with peaks in May and October. The discrepancy between the SST anomaly and SSHA would suggest that the seasonal SST anomaly variations would represent only a thin surface layer so that their steric height changes do not affect the SSHA. Indeed, the reported seasonal changes of the vertical temperature profile in the Makassar Strait in [23] behave differently from these seasonal SST anomaly variations.

These seasonal variations are then quantitatively investigated in the dynamic equation of motion. Assuming the Coriolis force is negligible near the Equator, the equation of motion for the along-strait component in the upper layer can be written as the balance

between the acceleration, the pressure gradient force, the wind stress, and the bottom friction terms: namely,

$$\frac{du}{dt} = -g \frac{\partial \eta}{\partial x} + \frac{\tau}{\rho h} - \frac{ru}{h}, \quad (1)$$

where u is the layer-averaged along-strait velocity component, $\frac{\partial \eta}{\partial x}$ the along-strait SSH gradient, g the acceleration of gravity, τ the along-strait wind stress component, ρ the density of seawater, h the water depth, and r the linear bottom friction coefficient. Since the ITF velocity is not significantly strong, the equation can be linearized by removing the advection term, which allows us to discuss the seasonal component separately. Applying to the upper layer of the southern Makassar Strait near the Labani Channel, seasonal variations of these terms are calculated and plotted in Figure 5, using $g = 9.8 \text{ m s}^{-2}$, $\rho = 1.03 \times 10^3 \text{ kg m}^{-3}$, $h = 50 \text{ m}$, $r = 1.5 \times 10^{-4} \text{ m s}^{-1}$, u = the ITF velocity at the 40 m depth, and $\frac{\partial \eta}{\partial x}$ = the SSH gradient between 1°S and 4°S , the closest pair to the mooring site (Figure 1). Note that the bottom friction coefficient r is not a determinant value, so we keep its typical order of magnitude as 10^{-4} m s^{-1} [24] and inductively determined the fraction of r to obtain reasonable variation ranges is in Figure 5.

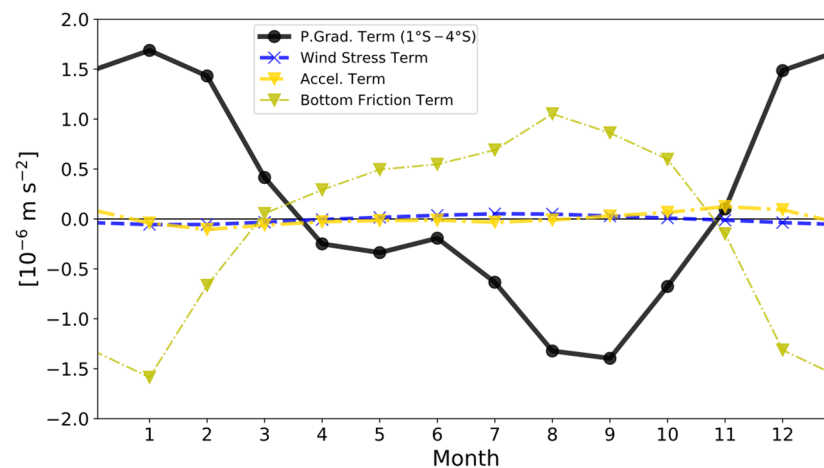


Figure 5. Mean seasonal variations of the terms in Equation (1) in 10^{-6} m s^{-2} unit. A black solid line shows the pressure gradient term between 1°S and 4°S (the first term on the right-hand side). A blue broken line shows the along-track wind stress term (the second term on the right-hand side). Yellow and green chain lines are for the acceleration and bottom friction terms (the term on the left-hand side and the third term on the right-hand side), respectively, determined from the along-strait ITE velocity component at the 40 m depth. All values are defined as positive in the northward.

Both wind stress and bottom friction terms have reversed phases with the pressure gradient term so that both can be qualitatively balanced with the pressure gradient term (Figures 4 and 5). However, the magnitude of the wind stress term in Figure 5 is significantly smaller than that of the other terms. Since the SSH gradients are not uniform within the Makassar Strait, as suggested in Figure 3b, the pressure gradient term could be smaller than one plotted in Figure 5 if we include areas other than the Labani Channel. Still, however, the pressure gradient term is too large with respect to the weak wind stress over the Makassar Strait. Note that the dynamic term balances investigated for the MJO in [2] are of the order of 10^{-8} m s^{-2} , which are close to that of the wind stress term shown in Figure 5. In other words, the seasonal SSH gradient in the Makassar Strait, seen in Figure 3, is significantly larger than the SSH gradient seen in the MJO, and only the bottom friction term would balance this large seasonal pressure gradient term. Note that both wind stress and bottom friction terms include the depth h so that their magnitude ratio does not depend on h . The selection of h would affect the balance between the bottom friction term and the pressure gradient term, but it also depends on the non-determinant parameter r .

Note that the acceleration term in Figure 5 is not only too small but also its phase is shifted from that of the other terms, as its maximum value appears in November, in which the other terms become almost zero. This would suggest that the ITF velocity is not directly accelerated by a single term in Equation (1).

4. Variations around the Makassar Strait

In the previous section, we have seen that the seasonal SSHA variations are in phase over the whole Makassar Strait, with their amplitude strengthened in the southern part, as suggested by [5]. To examine this tendency outside the Makassar Strait, we have applied the same processes (i.e., nine cycle and five points smoothing 10-month and 13-month Gaussian filters and monthly averaging over 17 years) to obtain the mean seasonal SSHA variations at additional 50 points in and around the Makassar Strait (the Celebes Sea, the Java Sea, the Flores Sea, the southwestern Pacific Ocean, and the northeastern Indian Ocean) together with four points in Figure 3a. Then, CC with the seasonal SSHA variation at the point 5°S, 117.3°E (shown in Figure 2b) is calculated for each point (Table 2). Figure 6 shows the spatial distributions of CC. The CC is colored with criteria values 0.98, 0.90, and 0.57, which are selected so that the CC differences (0.98 and 0.90, or 0.90 and 0.57) become significant with a 99% confidence level using Fisher's Z-test with 12 monthly samples.

Table 2. Locations of the selected 54 points in the Makassar Strait, Celebes Sea, Java Sea, Flores Sea, Pacific and Indian Ocean. Pearson Correlation Coefficients (CC) with the seasonal SSH variations at point “M” (5°S, 117.3°E; Point Number 18) are also shown, together with satellite Track numbers.

(a) Pacific Ocean				
Number	Track	Lat [°N]	Lon [°E]	CC
1	177	8.1	128.3	−0.93
2 *	177	6.5	127.8	−0.97
3	177	5.5	127.4	−0.94
* marked as “P” in Figure 6.				
(b) Celebes Sea				
Number	Track	Lat [°N]	Lon [°E]	CC
4 *	101	5.0	124.4	0.26
5	101	4.0	124.0	0.68
6	101	3.0	123.7	0.90
7	101	2.0	123.3	0.81
8	25	4.0	121.2	0.47
9	25	3.0	120.8	0.54
10 †	190	2.0	120.5	0.94
11	190	3.0	120.1	0.69
12	190	4.0	119.7	0.24
13	203	3.5	118.2	0.85
* marked as “C” in Figure 6. † shown in Figure 3a.				
(c) Makassar Strait				
Number	Track	Lat [°N]	Lon [°E]	CC
14	114	0.0	118.3	0.97
15 †	114	−0.9	118.7	0.99
16 †	25	−4.0	118.3	0.97
17	38	−4.5	117.1	1.00
18 *†	38	−5.0	117.3	1.00
19	25	−5.0	118.0	0.97

Table 2. Cont.

* marked as “M” in Figure 6. † shown in Figure 3a.				
(d) Java Sea				
Number	Track	Lat [°N]	Lon [°E]	CC
20	216	−6.0	114.8	0.78
21	216	−7.4	115.4	0.87
22	216	−7.9	115.5	0.78
23	216	−8.4	115.7	0.89
24 *	25	−7.9	116.9	0.30
25	25	−7.0	117.3	0.81
26	38	−6.0	117.7	1.00
27	38	−7.0	118.0	0.69
* marked as “L” in Figure 6.				
(e) Flores Sea				
Number	Track	Lat [°N]	Lon [°E]	CC
28	38	−7.9	118.4	0.21
29	101	−7.9	119.7	0.16
30	101	−7.0	120.1	0.93
31	114	−6.5	120.7	0.98
32	101	−5.0	120.8	0.95
33	114	−8.0	121.2	0.47
34	177	−7.9	122.6	0.24
35	177	−7.0	122.9	0.86
36	177	−6.0	123.3	0.96
(f) Indian Ocean				
Number	Track	Lat [°N]	Lon [°E]	CC
37	101	−9.0	119.4	0.82
38 *	203	−9.5	113.5	0.96
39	177	−9.5	122.0	0.96
40	216	−10.0	116.3	0.98
41	101	−10.5	118.8	0.94
42	38	−10.5	119.3	1.00
43	203	−11.0	113.0	0.53
44	25	−11.0	115.8	0.72
45	216	−11.0	116.7	0.84
46	101	−11.0	118.6	0.86
47	38	−11.0	119.5	0.98
48	177	−11.0	121.5	0.89
49 †	203	−12.0	112.6	−0.45
50	25	−12.0	115.4	−0.34
51	216	−12.0	117.0	−0.50
52	101	−12.0	118.2	−0.19
53	38	−12.0	119.9	0.21
54	177	−12.0	121.1	0.30
* marked as “J” in Figure 6. † marked as “I” in Figure 6.				

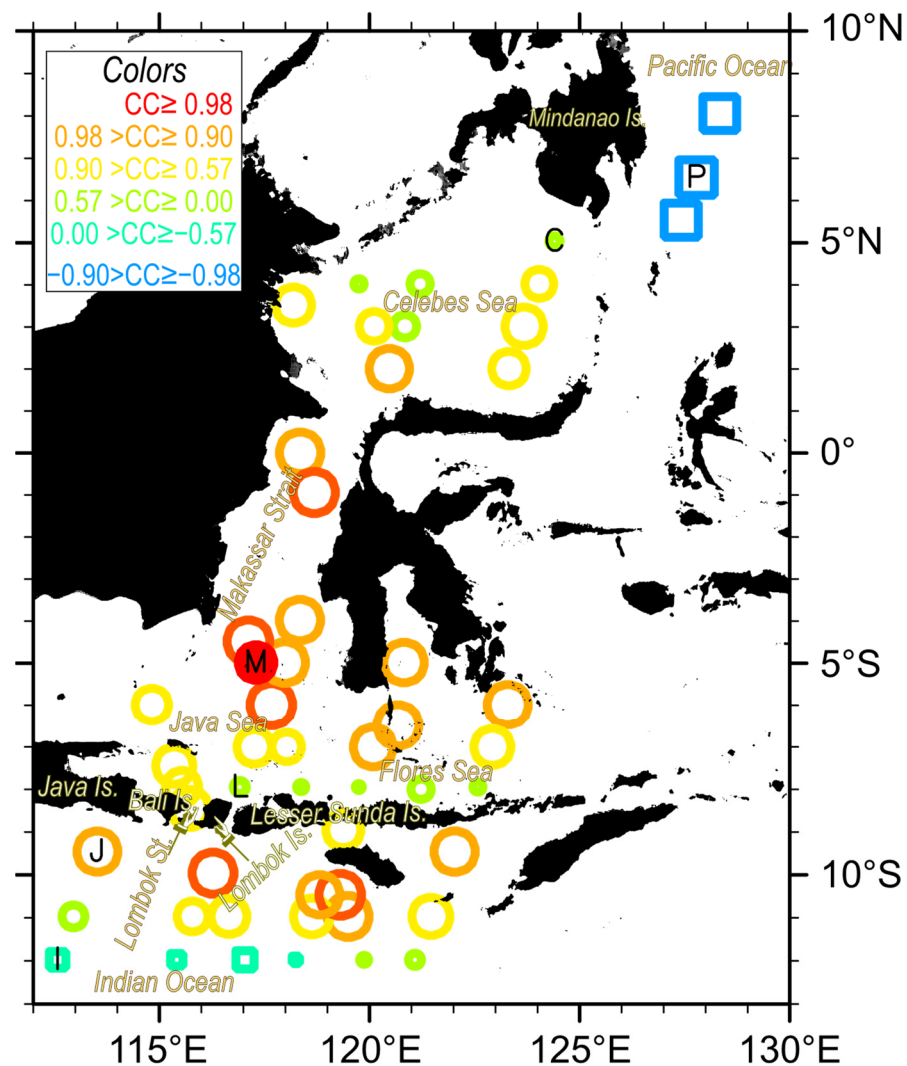


Figure 6. Distribution of Pearson correlation coefficients (CC) with the mean seasonal SSH variations at the point in the Makassar Strait, marked as “M”. Positive correlations are shown with circles, while negative correlations are shown with squares. The size of circles or squares depends on the magnitude of the coefficient. Marks are plotted with red (≥ 0.98), orange (0.9 to 0.98), yellow (0.57 to 0.9), light green (0 to 0.57), turquoise blue (-0.57 to 0), cyan (-0.9 to -0.57), light blue (-0.98 to -0.9) and deep blue (< -0.98). The location and values of CC are listed in Table 2.

All data points within the Makassar Strait, including three points not included in Figure 3a, are in phase so that their correlation coefficient is larger than 0.97 (red and orange circles in Figure 6). In the Celebes Sea, however, the distribution of CC is different in the northern and southern parts. The largest CC = 0.94 is found at 2°N, 120.5°E (Point Number 10), the closest point to the northern Makassar Strait (red circle in Figure 1), then moderate CC values larger than 0.57 (yellow circles) are present in the southern Celebes Sea. However, in the northern Celebes Sea where is away from the Makassar Strait, CC decreases as lower than 0.54 (green circles). For example, the point in the northeastern Celebes Sea at 5°N, 124.4°E (Point Number 4; marked as “C” in Figure 6) has small CC = 0.26 (Table 2). Similarly, in the northern Java Sea, CC becomes smaller as the distance from the Makassar Strait increased.

In the Flores Sea, contrasts between the northern and southern parts become clearer. In the northern part, CC values are larger than 0.9, as shown by orange circles in Figure 6, even at points far from the Makassar Strait. However, CC values along the northern coast of the Lesser Sunda Islands in the southern part of the Flores Sea are significantly low, as

shown using small green circles. The low CC value along the northern coast is also seen in the southern Java Sea, as CC is only 0.30 at the point northeast of Lombok Island, 7.9°S, 116.9°E (Point Number 24; marked as “L”).

On the contrary, high CC values are found along the southern coast of the Java and Lesser Sunda Islands. Those high CC values are, however, confined only near the coasts so that offshore points in the Indian Ocean show small or weakly negative correlations. The point south of Java Island at 9.5°S, 113.5°E (Point Number 38; marked as “J”) has a significantly high CC = 0.96, but its 300 km offshore point at 12°S, 112.6°E (Point Number 49; marked as “I”) has a negative CC = −0.41.

More significant negative correlations are found in the southwestern Pacific Ocean. The CC = −0.96 is found at the point 6.5°N, 127.8°E (Point Number 2), marked as “P” in Figure 6. Surrounding points similarly have significant negative correlations, as shown using light blue and cyan squares, in contrast to small positive CC values at the adjacent points in the northeastern Celebes Sea.

For more insight, the seasonal SSHA variations in the above six marked points are plotted in Figure 7. Clear in-phase relationships with the monsoon are found in the Makassar Strait (M; black line), along the southern coast of Java Island (J; red line), and oppositely in-phase in the southwestern Pacific Ocean (P; blue line). At other locations in the northern Celebes Sea (C; cyan chain line) and in the offshore Indian Ocean (I; orange broken line), their phases do not correspond to the monsoon seasons. Especially, the SSHA variations at the point northeast of Lombok Island (L; purple dotted line) have double peaks in May and December, which differ significantly from the SSHA variations in the Makassar Strait and are rather similar to the seasonal variations of the deep-layer ITF velocity shown in Figure 4.

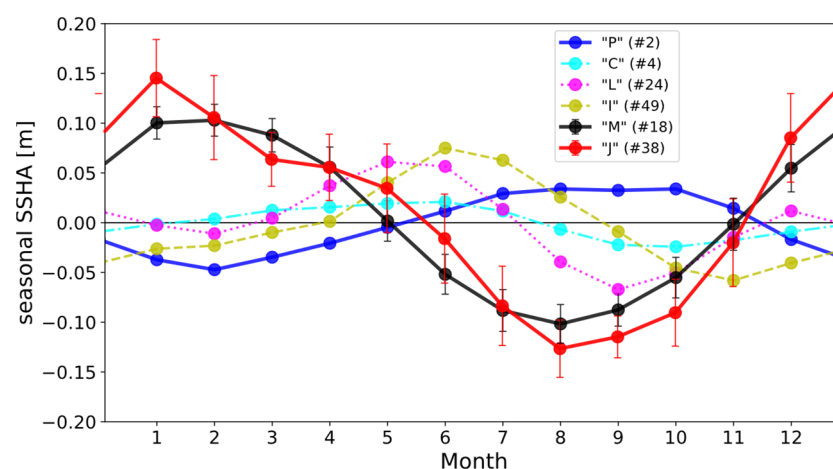


Figure 7. The mean seasonal SSHA variations at six points shown in Table 2; in the Makassar Strait (bold black line; marked using “M” in Figure 6), in the Pacific Ocean (bold blue line; “P”), south of Java Island (bold red line; “J”), in the Celebes Sea (cyan chain line; “C”), northeast of Lombok Island (purple dotted line; “L”), and in the Indian Ocean (orange broken line; “I”). The standard deviations are plotted using vertical bars for “M” and “J” points.

The SSHA difference between point “P” in the southwestern Pacific Ocean and point “J” south of Java Island would reach nearly 0.2 m, which is larger than the SSHA difference within the Makassar Strait shown in Figure 3b so that this SSHA difference will become a good index that is in-phase with the seasonal SSHA variations in the Makassar Strait. However, adjacent seasonal SSHA variations in the northern Celebes and southern Java Seas disconnect those SSHA variations in the Pacific and Indian Ocean, and therefore, the SSH difference between “P” and “J” points would not directly drive the SSHA gradient within Makassar Strait.

In Figure 7, the amplitude of the seasonal SSHA variations at the point “J” south of Java is slightly larger than that in the southern Makassar Strait “M”, although the range

discrepancy does not substantially exceed the standard deviations at the point “J”. As seen in Figure 7, the standard deviation at point “J” is significantly larger than that at point “M”, suggesting that the near-annual SSHA variations Z^{na} south of Java Island include large interannual variations than ones in the Makassar Strait, shown in Figure 2b.

To investigate spatial distributions of the amplitude of the seasonal SSHA variations that are in phase with the SSHA in the Makassar Strait, the least square fitting method is introduced. Namely, the seasonal SSHA variations at a given point, $\eta(t)$, would be written as

$$\eta(t) = A \eta_M(t) + \varepsilon(t), \quad (2)$$

where $\eta_M(t)$ is the seasonal SSHA variations at the point “M” (5°S, 117.3°E) in the Makassar Strait (Point Number 18 in Table 2), A is the amplitude factor of the fitted variations, and $\varepsilon(t)$ is the independent residual SSHA variations that are not in phase with η_M . The unknown A is determined to minimize the sum of squared difference $S = \sum_i [\eta(t_i) - A\eta_M(t_i)]^2$. Namely,

$$A = \frac{\sum_i \eta(t_i) \eta_M(t_i)}{\sum_i [\eta_M(t_i)]^2}. \quad (3)$$

The fitting would be meaningful only when the independent variations ε are negligibly small with respect to the fitted variations $A \eta_M$. Therefore, we introduce the dominance ratio d as the ratio of the variance of the fitted variations $A \eta_M(t)$ to the variance of the original SSHA variations $\eta(t)$; namely,

$$d = \frac{\sum_i [A\eta_M(t_i)]^2}{\sum_i [\eta(t_i)]^2}. \quad (4)$$

In other words, A would not be meaningful if d were not large enough. The amplitude factor A and the dominance ratio d are calculated for all 54 points (Table 3).

Table 3. The dominance ratio d in Equation (4) and the amplitude factor A in Equation (3) for the seasonal SSHA variations at Point Number 18 are calculated at the 54 points listed in Table 2.

(a) Pacific Ocean					
Number	Track	Lat [°N]	Lon [°E]	Amp. Factor	Dom. Ratio
1	177	8.1	128.3	−0.38	0.86
2	177	6.5	127.8	−0.38	0.94
3	177	5.5	127.4	−0.41	0.88
(b) Celebes Sea					
Number	Track	Lat [°N]	Lon [°E]	Amp. Factor	Dom. Ratio
4	101	5.0	124.4	0.05	0.07
5	101	4.0	124.0	0.18	0.46
6	101	3.0	123.7	0.30	0.81
7	101	2.0	123.3	0.29	0.65
8	25	4.0	121.2	0.06	0.22
9	25	3.0	120.8	0.13	0.29
10	190	2.0	120.5	0.31	0.89
11	190	3.0	120.1	0.19	0.48
12	190	4.0	119.7	0.06	0.06
13	203	3.5	118.2	0.15	0.72

Table 3. Cont.

(c) Makassar Strait					
Number	Track	Lat [°N]	Lon [°E]	Amp. Factor	Dom. Ratio
14	114	0.0	118.3	0.46	0.94
15	114	−0.9	118.7	0.55	0.97
16	25	−4.0	118.3	0.95	0.93
17	38	−4.5	117.1	1.05	1.00
18	38	−5.0	117.3	1.00	1.00
19	25	−5.0	118.0	0.82	0.95
(d) Java Sea					
Number	Track	Lat [°N]	Lon [°E]	Amp. Factor	Dom. Ratio
20	216	−6.0	114.8	0.82	0.61
21	216	−7.4	115.4	0.45	0.76
22	216	−7.9	115.5	0.31	0.60
23	216	−8.4	115.7	0.53	0.79
24	25	−7.9	116.9	0.16	0.09
25	25	−7.0	117.3	0.51	0.65
26	38	−6.0	117.7	0.91	0.99
27	38	−7.0	118.0	0.39	0.47
(e) Flores Sea					
Number	Track	Lat [°N]	Lon [°E]	Amp. Factor	Dom. Ratio
28	38	−7.9	118.4	0.06	0.04
29	101	−7.9	119.7	0.08	0.03
30	101	−7.0	120.1	0.69	0.87
31	114	−6.5	120.7	0.68	0.96
32	101	−5.0	120.8	0.76	0.90
33	114	−8.0	121.2	0.16	0.22
34	177	−7.9	122.6	0.10	0.06
35	177	−7.0	122.9	0.49	0.75
36	177	−6.0	123.3	0.78	0.92
(f) Indian Ocean					
Number	Track	Lat [°N]	Lon [°E]	Amp. Factor	Dom. Ratio
37	101	−9.0	119.4	0.67	0.67
38	203	−9.5	113.5	1.14	0.92
39	177	−9.5	122.0	0.99	0.93
40	216	−10.0	116.3	0.80	0.96
41	101	−10.5	118.8	0.73	0.88
42	38	−10.5	119.3	0.93	0.99
43	203	−11.0	113.0	0.31	0.28
44	25	−11.0	115.8	0.43	0.52
45	216	−11.0	116.7	0.44	0.70
46	101	−11.0	118.6	0.50	0.74
47	38	−11.0	119.5	0.58	0.96
48	177	−11.0	121.5	0.46	0.79
49	203	−12.0	112.6	−0.25	0.21
50	25	−12.0	115.4	−0.15	0.11
51	216	−12.0	117.0	−0.14	0.25
52	101	−12.0	118.2	−0.07	0.04
53	38	−12.0	119.9	0.05	0.04
54	177	−12.0	121.1	0.07	0.09

By substituting Equation (3) to (4), d can be transformed as:

$$d = \frac{[\sum_i \eta(t_i) \eta_M(t_i)]^2}{\sum_i [\eta_M(t_i)]^2 \sum_i [\eta(t_i)]^2} = CC^2. \quad (5)$$

As expected from Equation (5), the characteristics of d are close to those of CC in Table 2. Namely, both d and the magnitude of CC are high within the Makassar Strait, along the southern coast of the Java and Lesser Sunda Islands, in the northern Java and Flores Seas, and in the southwestern Pacific Ocean. On the contrary, they are significantly small along the northern coast of the Lesser Sunda Islands (in the southern Java and Flores Seas). Hereinafter, we will mainly use points whose d exceeds 0.8 or CC exceeds 0.89 to investigate the spatial distribution of A . Points with d exceeding 0.64 or CC exceeding 0.80 are supplementary used.

The distribution of A is mapped in Figure 8 as the sizes of markers. In the Makassar Strait and adjacent northern Java and southern Celebes Seas, the northward decreasing tendency is confirmed, as explained in Figure 3a. More precisely, the maximum $A = 1.05$ is found at 4.5°S , 117.1°E (Point Number 17 in Table 3), near the edge of 50 m isobath (Figure 1). As the distance from this point increases, the amplitude A becomes smaller. This tendency is still found in the northern part of the Makassar Strait (north of 3°S) as $A = 0.55$ to 0.46 , and even in the southern Celebes Sea as $A = 0.31$ to 0.30 , although the decreasing ratio of A is significantly smaller than that in the southern part of the Makassar Strait. This confirms that the largest horizontal SSHA gradient by this in-phase seasonal variation would occur in the Makassar Strait between 4°S and 1°S over the narrow Labani Channel.

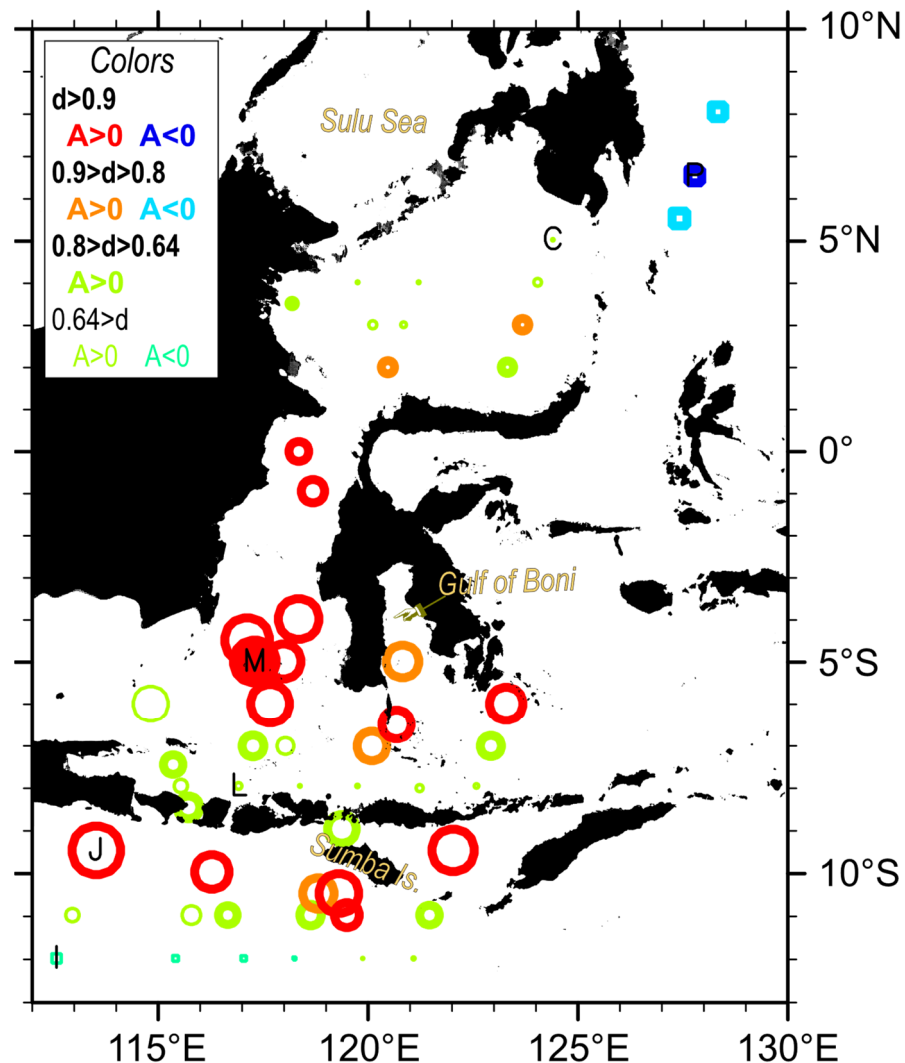


Figure 8. The amplitude factor A in Equation (3) is indicated using the size of each plot. The red circle marked as “M” is the reference point of η_M , showing the unity $A = 1.00$. Plots are colored with red or deep blue when the dominance ratio d exceeds 0.90, orange or light blue when d exceeds 0.80, and green when d is below 0.80. Bold lines are used to show points whose d is larger than 0.64.

On the other hand, in the northern part of Flores Sea east of 120°E and north of 7°S, the maximum $A = 0.78$ is found at the eastern point 6°S, 123.3°E (Point Number 36), while the second largest $A = 0.76$ is at 5°S, 120.8°E (Point Number 32), in the Gulf of Boni south of Sulawesi Island. These distributions in the northern Flores Sea do not follow the distance-determined relationship seen in the Makassar Strait, and it rather suggests that the distance from coasts of large islands determines the magnitude of A . Similarly, in the Indian Ocean, points with larger d are confined to coastal areas south of Java and the Lesser Sunda Islands. Extra-large $A = 1.14$ is found at 9.5°S, 113.5°E (Point Number 38), south of Java Island, marked using “J” in Figure 8, but no significant η_M components are found at the offshore point (11°S, 113°E; Point Number 43) that is 170 km away from point “J”. Around 119°E and along the southern coast of Sumba Island, maximum $A = 0.93$ occurs at a point 10.5°S, 119.3°E (Point Number 42) closest to the island, then A decreases to 0.73 (10.5°S, 118.8°E; Point Number 41) and 0.58 (11°S, 119.5°E; Point Number 47), and A becomes 0.50 at the offshore point 11°S, 118.6°E (Point Number 46).

Together with their in-phase relationship with the monsoon seasons, the coastally confined characteristics in Figure 8 in the Indian Ocean and in the northern Flores Sea would suggest that these SSHA variations are caused by the divergence or convergence of surface wind-driven transport by coastal walls of large islands. Namely, during the northwest (or southeast) monsoon period from December to March (June to September), the eastward (westward) wind component is found over these areas, producing an increase (decrease) of SSH along the southern coast of large islands.

Similarly, within the Makassar Strait, although the maximum amplitude A is found away from the coastal wall boundaries of large islands, wind-driven currents over shallow areas can also generate SSHA gradients, especially when the depth is as shallow as the surface boundary layer thickness [25]. This would explain why the largest SSHA variations in the Makassar Strait occur at the southern shallow point.

In the Pacific Ocean, all three points have significant d and similar negative A values. These points are also far from the coastal walls of large islands, but variations in wind speeds and the Coriolis parameter can produce the convergence or divergence of wind-driven transport. Namely, during the northwest (or southeast) monsoon period from December to March (June to September), both enhanced Coriolis parameter and higher southwestward (northeastward) wind speeds at higher latitudes would produce divergence (convergence) of wind-driven transport at those points, resulting in lower (higher) SSHA variations.

5. Discussion

If the convergence or divergence of wind-driven transport by coastal walls is the dominant factor along the southern coast of the Lesser Sunda Islands, the reversed in-phase relationship could be symmetrically expected on the northern coast, accounting for large spatial scales of wind directions. Namely, negative A values with large d could be present along the northern coast of the Lesser Sunda Islands in Figure 8, as seen at points in the Pacific Ocean. However, their d values are found to be significantly small (Table 3). We recall that the actual seasonal SSHA variations at the point “L” (7.9°S, 116.9°E; Point Number 24) have intra-seasonal variations with double peaks in May and December (Figure 7), which are significantly different from the monsoon seasons. This suggests that other significant factors than the convergence of local wind-driven transports should be present in the southern part of the Java and Flores Seas.

The same least square fit in Equation (2) but using the seasonal SSHA variations at the point “L” (Point Number 24) instead of η_M is plotted in Figure 9 and is listed in Table 4. Only three points have significant d values, all of which are along the northern coast of the Lesser Sunda Islands and only to the east of point “L” (Figure 9). To the northwest of the Lombok Strait, no points have significant dominance ratio d , except a point to the north of Bali Island (7.9°S, 115.5°E; Point Number 22) with moderate $d = 0.69$ (or CC = 0.83). This suggests the existence of different signals to the west and east of the Lombok Strait. Past studies on intra-seasonal variations in the Indonesian Seas (e.g., [26–28]) suggest different

propagation routes of the Kelvin waves in the Java and Flores Seas. Some of the Kelvin waves propagating eastward along the southern coast of Java and Bali islands enter the Java Sea through the Lombok Strait and propagate westward along the northern coast of Bali Island and then northeastward toward Kangean Island along shallow isobaths (Figures 1 and 9). The other part of the Kelvin waves continue propagating along the southern coast of the Lesser Sunda Islands and enter the Flores Sea through the Ombai Strait, and they propagate westward along the northern coast [28]. At the point “L”, therefore, the Kelvin waves would take the latter route along the northern coast of the Lesser Sunda Islands, only to the east of the Lombok Strait. Note that in the offshore Indian Ocean in Figure 9, a long train of points with moderate d is found along 11°S or 12°S , even to the east of the Lombok Strait.

In this study, only near-annual variations are focused, partly because the aliased K_1 constituent (173 days period) could contaminate altimetry-derived SSHA variations. However, intra-seasonal components are found in Figure 7 at the point “L”. The Gaussian filter works well to remove sinusoidal variations, such as aliased tidal constituents, but is less effective for signals with a larger kurtosis, such as intermittent pulses. Therefore, although variations shorter than 10 months are mostly filtered out in this study, significantly large intermittent pulses would not be fully removed using the Gaussian filter so that they could remain in the near-annual data. In order to confirm this, the near-annual variations Z^{na} at the point “L” are plotted in Figure 10. They include pulse-like short-term SSHA changes, which are not observed in Figure 2a in the Makassar Strait. The RMS values for short-term variations Z^S , near-annual variation Z^{na} , and long-term variations Z^L at the point “L” are 0.17 m, 0.04 m, and 0.03 m, respectively, which confirms that the short-term variations are significantly large at the point “L”. It should be also noted that most of these pulses in Figure 10 are phase-locked in the annual year days. We recall that the aliased K_1 constituent are not phase-locked in the annual year days as seen as Z^S in Figure 2a, so that the aliased K_1 tidal errors would be removed in the mean seasonal SSHA variations η .

The near-annual SSHA variations Z^{na} at another point south of Kangean Island (7.4°S , 115.4°E ; Point Number 21) are also plotted in Figure 10 for reference. This point is along the suggested pathway of the Kelvin waves from the Lombok Strait (Figure 9). Since the dominance ratio $d = 0.49$ ($\text{CC} = 0.7$) is small at this point, the SSHA variations should include some independent variations that are not in phase with the SSHA variations at point “L”. The near-annual SSHA variations Z^{na} at Point Number 21 also include pulses but with different phases from the ones at point “L”. These results are consistent with the concept of different pathways of the Kelvin waves.

Table 4. The same as Table 3, but for another reference point, “L” (Point Number 24).

(a) Pacific Ocean					
Number	Track	Lat [$^{\circ}\text{N}$]	Lon [$^{\circ}\text{E}$]	Amp. Factor	Dom. Ratio
1	177	8.1	128.3	−0.42	0.29
2	177	6.5	127.8	−0.29	0.15
3	177	5.5	127.4	−0.02	0.00
(b) Celebes Sea					
Number	Track	Lat [$^{\circ}\text{N}$]	Lon [$^{\circ}\text{E}$]	Amp. Factor	Dom. Ratio
4	101	5.0	124.4	0.36	0.77
5	101	4.0	124.0	0.22	0.19
6	101	3.0	123.7	0.26	0.17
7	101	2.0	123.3	0.39	0.32
8	25	4.0	121.2	0.19	0.54
9	25	3.0	120.8	0.09	0.04
10	190	2.0	120.5	0.34	0.29
11	190	3.0	120.1	0.29	0.32
12	190	4.0	119.7	0.32	0.39
13	203	3.5	118.2	0.17	0.23

Table 4. Cont.

(c) Makassar Strait					
Number	Track	Lat [°N]	Lon [°E]	Amp. Factor	Dom. Ratio
14	114	0.0	118.3	0.23	0.06
15	114	−0.9	118.7	0.38	0.12
16	25	−4.0	118.3	0.62	0.11
17	38	−4.5	117.1	0.59	0.08
18	38	−5.0	117.3	0.59	0.09
19	25	−5.0	118.0	0.74	0.20
(d) Java Sea					
Number	Track	Lat [°N]	Lon [°E]	Amp. Factor	Dom. Ratio
20	216	−6.0	114.8	1.21	0.36
21	216	−7.4	115.4	0.71	0.49
22	216	−7.9	115.5	0.64	0.69
23	216	−8.4	115.7	0.74	0.41
24	25	−7.9	116.9	1.00	1.00
25	25	−7.0	117.3	0.99	0.65
26	38	−6.0	117.7	0.51	0.08
27	38	−7.0	118.0	0.73	0.44
(e) Flores Sea					
Number	Track	Lat [°N]	Lon [°E]	Amp. Factor	Dom. Ratio
28	38	−7.9	118.4	0.52	0.89
29	101	−7.9	119.7	0.90	0.94
30	101	−7.0	120.1	0.80	0.31
31	114	−6.5	120.7	0.40	0.09
32	101	−5.0	120.8	0.85	0.30
33	114	−8.0	121.2	0.49	0.55
34	177	−7.9	122.6	0.78	0.85
35	177	−7.0	122.9	0.78	0.50
36	177	−6.0	123.3	0.83	0.27
(f) Indian Ocean					
Number	Track	Lat [°N]	Lon [°E]	Amp. Factor	Dom. Ratio
37	101	−9.0	119.4	1.01	0.41
38	203	−9.5	113.5	1.10	0.23
39	177	−9.5	122.0	0.72	0.13
40	216	−10.0	116.3	0.73	0.21
41	101	−10.5	118.8	0.86	0.32
42	38	−10.5	119.3	0.69	0.15
43	203	−11.0	113.0	0.98	0.76
44	25	−11.0	115.8	0.94	0.65
45	216	−11.0	116.7	0.57	0.32
46	101	−11.0	118.6	0.80	0.51
47	38	−11.0	119.5	0.55	0.23
48	177	−11.0	121.5	0.53	0.28
49	203	−12.0	112.6	0.58	0.29
50	25	−12.0	115.4	0.67	0.58
51	216	−12.0	117.0	0.26	0.22
52	101	−12.0	118.2	0.61	0.71
53	38	−12.0	119.9	0.38	0.76
54	177	−12.0	121.1	0.35	0.62

Note that semi-annual components are also found in the ITF velocity at the 300 m depth (Figure 4), which are suggested to be related to the intra-seasonal Kelvin wave propagations in the southern part of the Java Sea [23]. However, we do not quantitatively focus on these intra-seasonal variations and leave them for future studies since the intra-

seasonal variations would be significantly underestimated in this study by applying the Gaussian filters.

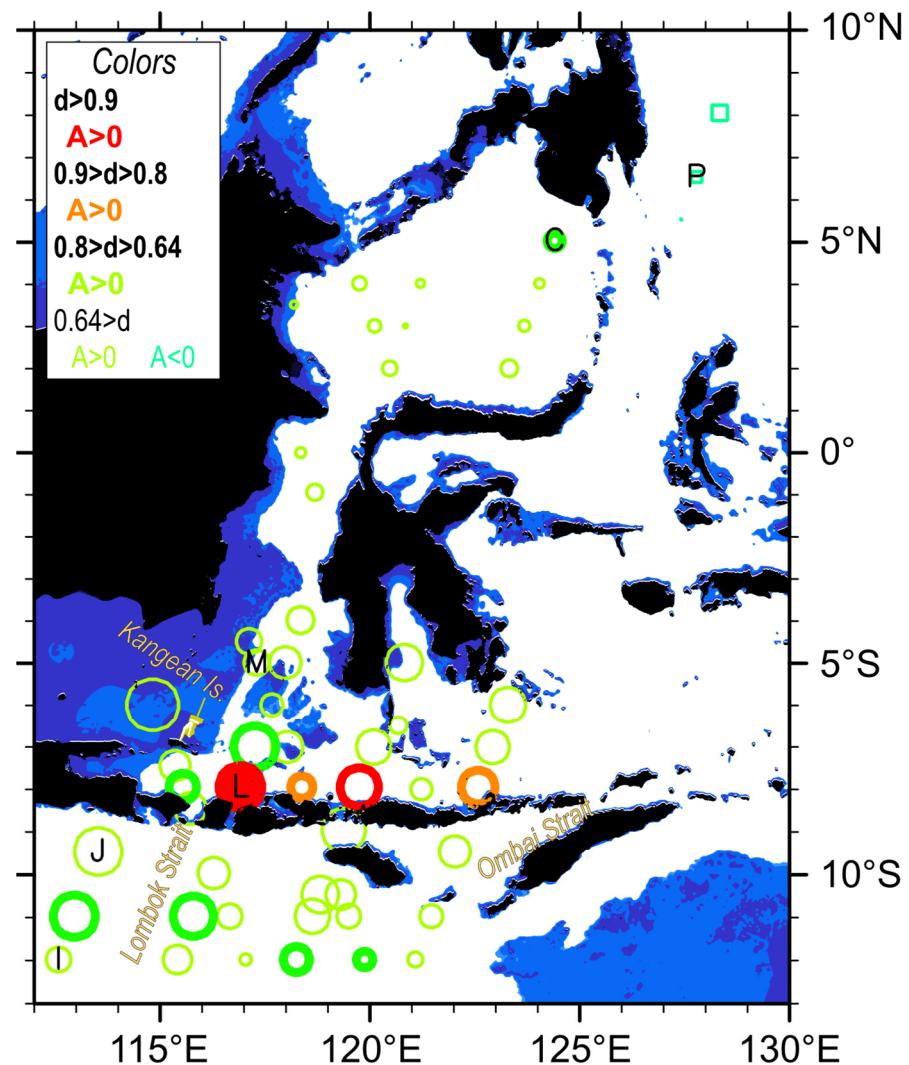


Figure 9. The same as Figure 8, but for another reference point, “L” (Point Number 24). Bottom topography contours at the 50 m and 300 m depths shown in Figure 1 are plotted for reference.

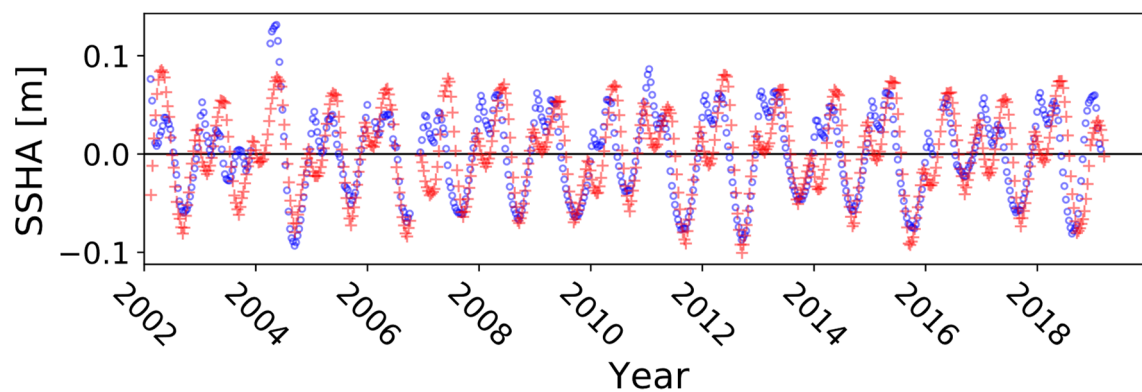


Figure 10. Near-annual SSHA variations Z^{na} at the point “L” (Point Number 24) east of the Lombok Strait (red crosses) and at the point $7.4^{\circ}\text{S } 115.4^{\circ}\text{E}$ (Point Number 21) south of Kangean Island, along the pathway of the Kelvin waves from the Lombok Strait (blue circles).

Some researchers suggest the potential contribution of injection of distinct water mass from the South China Sea into the southern Makassar Strait through the Java Sea (South China Sea throughflow, e.g., [29–31]), but this contribution cannot be discussed in this study since the injection paths are over the shallow areas where no SSHA data points are available. However, in Figure 8, significant d values for the mean seasonal SSHA variations η_M in the southern Makassar Strait are found even in the southern Celebes Sea, which cannot be explained using the South China Sea throughflow alone. Instead, note that points in the northern Celebes Sea have significantly smaller d values, which could be affected by inflow from the Sulu Sea.

6. Summary and Conclusions

Using along-track Jason-series data from 2002 to 2019 processed with the ALES re-tracker that can produce better-quality SSH observations in coastal areas, the mean seasonal SSH variations in and around the Makassar Strait are investigated. All data points are processed without spatial grid interpolation so that they can independently observe small-scale features around narrow straits and bays without producing pseudo signals by over-smoothing from far data points, although data point distributions become irregular.

The seasonal SSHA variations are confirmed in phase with the monsoon seasons at all points from the southern Celebes Sea to the northern Java Sea through the Makassar Strait. By applying the least square fitting of the seasonal SSHA variations at a point in the Makassar Strait, the largest amplitude of the in-phase variations is found at a point near the southern end of the Makassar Strait and near the 50 m isobath. As the distance from this point increases, the amplitude becomes smaller, producing horizontal SSHA gradients, i.e., the pressure gradient forces. The SSHA gradients are not uniform over the area, and the largest gradient is found between 4°S and 1°S in the Makassar Strait, over the narrow Labani Channel.

Since the pressure gradient force in the Makassar Strait is reversely in phase with the along-strait wind stress and the bottom friction of the surface ITF velocity, both can qualitatively balance with the pressure gradient force. Quantitatively, however, the wind stress is found too weak (approximately $0.5 \times 10^{-8} \text{ m s}^{-2}$) to balance the pressure gradient force (approximately $1.5 \times 10^{-6} \text{ m s}^{-2}$), suggesting that the pressure gradient force in the Makassar Strait is balanced with the bottom friction of the surface ITF velocity over the shallow-depth area, which is a significant topographic characteristic of this strait.

Similar in-phase seasonal SSHA variations are also found along the southern coast of Java and Lesser Sunda Islands, in the northern Flores Sea, and reversely in-phase in the southwestern Pacific Ocean. The areas in the Pacific and Indian Ocean are, however, isolated from the Makassar Strait by adjacent areas with uncorrelated SSHA variations, and thus, they do not directly force the SSHA gradient within the Makassar Strait. All of those in-phase seasonal SSHA variations would be caused by the convergence or divergence of local wind-driven transports.

Along the northern coast of the Lesser Sunda Islands, significant intra-seasonal SSHA variations are found, which could be related to the semi-annual ITF variations in the lower layer. However, since this study focuses on the mean seasonal variations, both intra-seasonal variations and interannual variations with ENSO and IOD events would be left for future studies.

These results can be summarized in short:

- Seasonal monsoon wind variations produce seasonal SSHA changes along coastal walls of large islands or over shallow areas.
- All those SSHA variations are in phase, even though they are generated independently.
- Large in-phase SSHA variations occur south of Java Island, while reversed in-phase variations are generated in the southwestern Pacific Ocean. Therefore, we can obtain a clear in-phase index by taking the difference between those SSHA variations.
- Along the northern coast of the Lesser Sunda Islands and in the northern Celebes Sea, the seasonal SSHA variations are out of phase from the monsoon seasons. Therefore,

the SSHA variations in the Pacific and Indian Ocean are dynamically isolated from the seasonal SSHA variations within the Makassar Strait using uncorrelated SSHA variations in the adjacent areas.

- In an area from the northern Java Sea to the southern Celebes Sea through the Makassar Strait, the seasonal SSHA variations are in phase, but their amplitude decreases toward the north, producing horizontal SSHA gradients. The largest SSHA gradient is found between 4°S and 1°S in the Makassar Strait, over the narrow Labani Channel.
- The pressure gradient force caused by the SSHA gradient is balanced with the bottom friction of the surface ITF velocity in the Makassar Strait since the wind stress over the strait is too weak.

Funding: This research was partially funded by The Japan Society for the Promotion of Science (JSPS) KAKENHI (Grant Numbers JP18H03737, JP21H05178, JP21K19848, JP22H01301, JP20H05168).

Data Availability Statement: The data presented in this study are openly available in FigShare at <https://doi.org/10.6084/m9.figshare.24064608>.

Acknowledgments: Ganmeng Zhang significantly helped the preparation of the data. Hiroyuki Tomita kindly provided information about the J-OFURO data set.

Conflicts of Interest: The author declares no conflict of interest.

References

1. Gordon, A.L.; Napitu, A.; Huber, B.A.; Gruenburg, L.K.; Pujiana, K.; Agustadi, T.; Kuswardani, A.; Mbay, N.; Setiawan, A. Makassar Strait Throughflow Seasonal and Interannual Variability: An Overview. *J. Geophys. Res. Oceans* **2019**, *124*, 3724–3736. [CrossRef]
2. Napitu, A.M.; Pujiana, K.; Gordon, A.L. The Madden-Julian Oscillation's Impact on the Makassar Strait Surface Layer Transport. *J. Geophys. Res. Oceans* **2019**, *124*, 3538–3550. [CrossRef]
3. Pujiana, K.; McPhaden, M.J.; Gordon, A.L.; Napitu, A.M. Unprecedented Response of Indonesian Throughflow to Anomalous Indo-Pacific Climatic Forcing in 2016. *J. Geophys. Res. Oceans* **2019**, *124*, 3737–3754. [CrossRef]
4. Susanto, R.D.; Song, Y.T. Indonesian throughflow proxy from satellite altimeters and gravimeters. *J. Geophys. Res. Oceans* **2015**, *120*, 2844–2855. [CrossRef]
5. Radjawane, I.M.; Azminuddin, F. Seasonal and semi-annual variability of sea surface height in Makassar Strait. *J. Phys. Conf. Ser.* **2016**, *739*, 012067. [CrossRef]
6. Ichikawa, K.; Yoshikawa, Y.; Morimoto, A.; Fukudom, K.; Yoon, J.H. Complementary Remote Sensing Observations of the Tsushima Warm Current Patterns. In *Remote Sensing of the Asian Seas*; Barale, V., Gade, M., Eds.; Springer: Cham, Switzerland, 2019; pp. 191–204.
7. Wang, X.; Ichikawa, K. Coastal Waveform Retracking for Jason-2 Altimeter Data Based on along-Track Echograms around the Tsushima Islands in Japan. *Remote Sens.* **2017**, *9*, 762. [CrossRef]
8. Gommenginger, C.; Thibaut, P.; Fenoglio-Marc, L.; Quartly, G.; Deng, X.; Gómez-Enri, J.; Challenor, P.; Gao, Y. Retracking Altimeter Waveforms Near the Coasts. In *Coastal Altimetry*; Vignudelli, S., Kostianoy, A.G., Cipollini, P., Benveniste, J., Eds.; Springer: Berlin/Heidelberg, Germany, 2011; pp. 61–101.
9. Wang, X.; Ichikawa, K.; Wei, D. Coastal Waveform Retracking in the Slick-Rich Sulawesi Sea of Indonesia, Based on Variable Footprint Size with Homogeneous Sea Surface Roughness. *Remote Sens.* **2019**, *11*, 1274. [CrossRef]
10. Ichikawa, K.; Wang, X.F.; Tamura, H. Capability of Jason-2 Subwaveform Retracker for Significant Wave Height in the Calm Semi-Enclosed Celebes Sea. *Remote Sens.* **2020**, *12*, 3367. [CrossRef]
11. Ichikawa, K.; Imawaki, S. Estimating the sea surface dynamic topography from Geosat altimetry data. *J. Oceanogr.* **1996**, *52*, 43–68. [CrossRef]
12. Yasui, T.; Abe, H.; Hirawake, T.; Sasaki, K.I.; Wakita, M. Seasonal pathways of the Tsugaru Warm Current revealed by high-frequency ocean radars. *J. Oceanogr.* **2022**, *78*, 103–119. [CrossRef]
13. Vignudelli, S.; Cipollini, P.; Gommenginger, C.; Snaith, H.; Coelho, H.; Fernandes, J.; Gomez-Enri, J.; Martin-Puig, C.; Woodworth, P.; Dinardo, S.; et al. The COASTALT Project: Towards an Operational use of Satellite Altimetry in the Coastal Zone. In Proceedings of the Oceans 2009, Biloxi, MS, USA, 26–29 October 2009.
14. Lumban-Gaol, J.; Adrian, D.; Vignudelli, S.; Leben, R.R.; Wayan Nurjaya, I.; Osawa, T.; Manurung, P.; Arhatin, R.E. An assessment of a coastal altimetry data product in the Indonesian Waters. *IOP Conf. Ser. Earth Environ. Sci.* **2018**, *176*, 012034. [CrossRef]
15. Hart-Davis, M.G.; Piccioni, G.; Dettmering, D.; Schwatke, C.; Passaro, M.; Seitz, F. EOT20: A global ocean tide model from multi-mission satellite altimetry. *Earth Syst. Sci. Data* **2021**, *13*, 3869–3884. [CrossRef]
16. Passaro, M.; Cipollini, P.; Vignudelli, S.; Quartly, G.D.; Snaith, H.M. ALES: A multi-mission adaptive subwaveform retracker for coastal and open ocean altimetry. *Remote Sens. Environ.* **2014**, *145*, 173–189.

17. Passaro, M.; Fenoglio-Marc, L.; Cipollini, P. Validation of Significant Wave Height from Improved Satellite Altimetry in the German Bight. *IEEE Trans. Geosci. Remote Sens.* **2015**, *53*, 2146–2156. [[CrossRef](#)]
18. Passaro, M.; Smith, W.; Schwatke, C.; Piccioni, G.; Dettmering, D. Validation of a global dataset based on subwaveform retracking: Improving the precision of pulse-limited satellite altimetry. In Proceedings of the OSTST Meeting 2017, Miami, FL, USA, 23–27 October 2017.
19. Gharineiat, Z.; Deng, X. Spectral Analysis of Satellite Altimeter and Tide Gauge Data around the Northern Australian Coast. *Remote Sens.* **2020**, *12*, 161. [[CrossRef](#)]
20. Andersen, O.B.; Knudsen, P. DNSC08 mean sea surface and mean dynamic topography models. *J. Geophys. Res.* **2009**, *114*. [[CrossRef](#)]
21. Gordon, A.L.; Huber, B.A. Data from: Makassar Strait Throughflow Seasonal and Interannual Variability: An Overview; Commons, C.U., Ed. 2019. Available online: <https://academiccommons.columbia.edu/doi/10.7916/d8-p78a-zm51> (accessed on 10 January 2023).
22. Tomita, H.; Hihara, T.; Kako, S.; Kubota, M.; Kutsuwada, K. An introduction to J-OFURO3, a third-generation Japanese ocean flux data set using remote-sensing observations. *J. Oceanogr.* **2019**, *75*, 171–194. [[CrossRef](#)]
23. Susanto, R.D.; Field, A.; Gordon, A.L.; Adi, T.R. Variability of Indonesian throughflow within Makassar Strait, 2004–2009. *J. Geophys. Res. Oceans* **2012**, *117*. [[CrossRef](#)]
24. Wang, D.; Zhang, J.; Wang, Y.P. Estimation of Bottom Friction Coefficient in Multi-Constituent Tidal Models Using the Adjoint Method: Temporal Variations and Spatial Distributions. *J. Geophys. Res. Oceans* **2021**, *126*, e2020JC016949. [[CrossRef](#)]
25. Kampf, J. Interference of wind-driven and pressure gradient-driven flows in shallow homogeneous water bodies. *Ocean Dynam* **2015**, *65*, 1399–1410. [[CrossRef](#)]
26. Sprintall, J.; Gordon, A.L.; Murtugudde, R.; Susanto, R.D. A semiannual Indian Ocean forced Kelvin wave observed in the Indonesian seas in May 1997. *J. Geophys. Res. Oceans* **2000**, *105*, 17217–17230. [[CrossRef](#)]
27. Iskandar, I.; Mardiansyah, W.; Masumoto, Y.; Yamagata, T. Intraseasonal Kelvin waves along the southern coast of Sumatra and Java. *J. Geophys. Res. Oceans* **2005**, *110*. [[CrossRef](#)]
28. Pujiana, K.; McPhaden, M.J. Intraseasonal Kelvin Waves in the Equatorial Indian Ocean and Their Propagation into the Indonesian Seas. *J. Geophys. Res. Oceans* **2020**, *125*, 18. [[CrossRef](#)]
29. Gordon, A.L.; Susanto, R.D.; Vranes, K. Cool Indonesian throughflow as a consequence of restricted surface layer flow. *Nature* **2003**, *425*, 824–828. [[CrossRef](#)] [[PubMed](#)]
30. Tozuka, T.; Qu, T.D.; Masumoto, Y.; Yamagata, T. Impacts of the South China Sea Throughflow on seasonal and interannual variations of the Indonesian Throughflow. *Dyn. Atmos. Oceans* **2009**, *47*, 73–85. [[CrossRef](#)]
31. Gordon, A.L.; Huber, B.A.; Metzger, E.J.; Susanto, R.D.; Hurlburt, H.E.; Adi, T.R. South China Sea throughflow impact on the Indonesian throughflow. *Geophys. Res. Lett.* **2012**, *39*. [[CrossRef](#)]

Disclaimer/Publisher’s Note: The statements, opinions and data contained in all publications are solely those of the individual author(s) and contributor(s) and not of MDPI and/or the editor(s). MDPI and/or the editor(s) disclaim responsibility for any injury to people or property resulting from any ideas, methods, instructions or products referred to in the content.